



## An investigation on quantitative detector characteristics of novel flexible skin dosimeter using Monte Carlo simulation method

Şenol Kaya<sup>1</sup>

### Keywords:

*Radiation sensors,  
Simulations,  
pyPENELOPE Code,  
Dosimeters*

**Abstract** — Novel lead oxide-based flexible dosimeters with superior performance were experimentally tested for electron therapy. However, absorbed/transmitted primary particle fraction and secondary radiation distribution from the dosimeter surface have not been reported. These features should be specified to improve the dosimeter's reliability for medical applications. Hence, the absorbed primary particle fraction, transmitted particle and secondary radiations distributions of lead oxide-based flexible skin dosimeter under the incident 6 MeV electron radiation have been investigated by pyPenelope Monte Carlo Simulation. The results have demonstrated that the generated secondary irradiation probabilities are not significantly high to enhance the therapeutic dose abnormally. In addition, the angular distribution of the scattered secondary irradiations is low. No abnormal changes were observed in the fraction and energy distribution of the transmitted primary electrons. Hence, it can be concluded that the designed structure has promising potential to be used as dosimeters in electron beam therapy.

### Subject Classification (2020):

## 1. Introduction

Ionising radiation is a useful tool for cancer treatment. Various photon and particle irradiations with different energies are used in radiation therapy [1-3]. The main aim is to prevent the death of cancer cells by protecting healthy tissue [4]. Controlling the photon radiation used in radiation therapy is difficult compared to the particle's irradiation, such as electron or proton. This is due to the high penetrating distance of photons which may also expose the deeper healthy tissues. Some malignant neoplasms or benign tumours can be localised on or close to the surface of the patient's skin, where electron beams can be effectively treated [5,6]. Electron beam therapy (EBT) can avoid exposing the deeper tissues by providing a high dose to the skin area [7]. Thus, possible side effects can be minimised.

The exposed dose of EBT value is also crucial for effectively treating the tumours. The treatment planning system estimates the therapeutic dose, which depends on the beam energy and penetration depth [8]. However, the treatment planning systems suffers from accuracy issues. The differences between the calculated and exposed skin dose may rise to  $\pm 20\%$  [9]. Therefore, a skin dosimeter is used to verify exposed skin dose in clinical applications. Optically stimulated luminescent dosimeters (OSLs),

<sup>1</sup>senolkaya52@gmail.com (Corresponding Author)

<sup>1</sup>Mehmet Tanrikulu Vocational School of Health Services, Abant İzzet Baysal University, Bolu, Türkiye  
Article History: Received: 15 Apr 2022 — Accepted: 24 Jun 2022 — Published: 31 Aug 2022

diode and MOSFET dosimeters are most commonly used in clinical practice to control the skin dose. These dosimeters measure the point dose during the EBT. Thus, the dose distributions on the whole skin region cannot be controlled. In addition, the skin surface is naturally curved, and positional accuracy of the dosimeters can affect the verification of the therapeutic doses in clinical practice. For instance, the MOSFET dosimeter exhibits sensitivity variations from 5% to 22.8% depending on its angular location during radiation therapy [10,11]. To overcome this issue, studies have focused on developing flexible dosimeters with functional materials [12-14]. The flexible dosimeter can be localised on the human body contours, which can precisely measure the cumulative skin dose. Han et al. [8] have fabricated lead oxide-based flexible skin dosimeters exhibiting superior performance in this aspect. It has also been reported that the PbO dosimeters show promising potential as semiconductor dosimeters instead of diodes.

Together with superior experimental electron radiation sensing characteristics of the PbO-based flexible dosimeters, some quantitative detector characteristics should be investigated for clinical applications. Scattering particles and the generation of secondary radiation are critical phenomena in radiation therapy [15]. These generated radiations can be entirely absorbed by the dosimeters or may backscatter on their surfaces. Penetration of the secondary radiation tissue level or absorption of the primary radiation in the dosimeter body may cause dose enhancement/decrement in the patient body [16,17]. Hence, the assessment of these quantitative detector characteristics should be considered in evaluating the clinical potential of the novel dosimeter. Monte Carlo simulation is a crucial tool to specify the possible density of scattered particles, generation of the secondary radiation and transmission ratio of the primary particles from the dosimeter structure. Various simulation packages, including Geant4, MCNPX, and pyPENELOPE, were composed to simulate the interactions between particles and the designed structure. Most of these simulation programs depend on multiple-scattering theories for electron transport to decrease the computational time [18].

Nevertheless, step length must be cautiously determined to decrease possible inaccuracies in the simulation results acquired from the designed dosimeter structure. The PENELOPE (Penetration and Energy Loss of Positrons and Electrons in the matter) Monte Carlo package has been preferred for the simulation of PbO-based flexible skin dosimeters since it does not lead to difficulties concerning the determination of proper step length [18,19]. The pyPENELOPE simulates the relevant interactions of the particles through the consistent differential cross sections [20]. During the simulation, pyPENELOPE runs the main code called Penepma. This package codes cover combined outcomes from first-principles calculations, semi-empirical formulations and estimated databases. The pyPENELOPE processes the most accurate physics concepts present that align with the intended generality of the code [20], which can be seen in Refs [21-23]. In this aspect, the density of scattered particles, generation of the secondary radiation and transmission ratio of the primary particles under 6 MeV electron radiations from the PbO-based flexible skin dosimeters structure have been investigated via open-source pyPENELOPE Monte Carlo code. Possible dose enhancement/decrement results in particle scattering/secondary radiation generation from designed skin dosimeters during clinical applications has also been discussed.

## 2. Materials and Methods

This simulation study was carried out via open source pyPENELOPE Monte Carlo code. As reported in [8] and relevant works in [24,25], the first layer was a 1 micrometre ( $\mu\text{m}$ ) thick gold electrode, the second layer was a 10  $\mu\text{m}$ -thick passive layer of C-type perylene, the third layer was 50  $\mu\text{m}$ -thick irradiation sensing layers of PbO, the fourth layer was 0.5  $\mu\text{m}$ -thick indium tin oxide, and the last base layer was 100  $\mu\text{m}$ -thick polyester substrates. These structures were designed by using the user-friendly interface of the pyPENELOPE software. The verification of the designed schematic structure was carried

out via `gview2d.exe`. The simulated lead oxide-based flexible dosimeter geometry is illustrated in Figure 1, and the simulated dosimeter structure reported in [8] is schematically depicted on the right bottom of Figure 1.

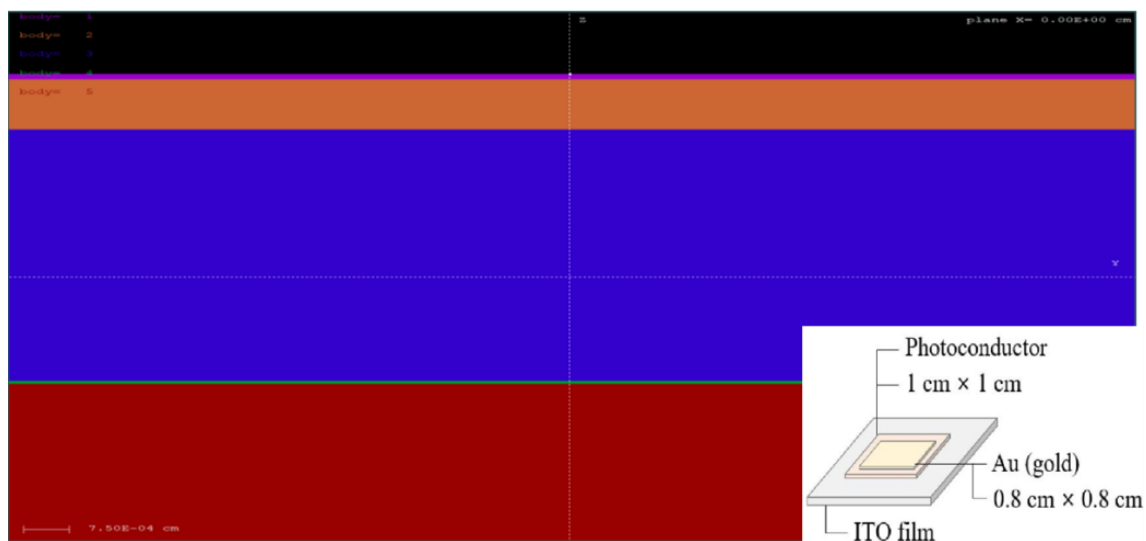


**Figure 1.** Simulated structure of the flexible skin dosimeter and the simulated dosimeter structure reported in [8]

Electron irradiations with various energies are used in electron beam therapy to treat tumour cells [3,6]. Among the different irradiation energies, the 6 MeV electrons are one of the most widely used electron beam therapy [6,26]. Hence, incident electron beam energy was set to 6 MeV during the evolution of the lead oxide-based flexible skin dosimeter. The numbers of  $8.2 \times 10^8$  electrons were simulated to decrease possible errors or uncertainties. The absorbed primary particle fractions, transmitted particles and secondary radiation distributions of flexible skin dosimeters under 6 MeV electron exposure were estimated via pyPENELOPE simulation. The simulations of the particles were controlled by C1, C2, WCC, and WCR. The C1 specifies the mean-free path among the hard inelastic incidents, while C2 determines the maximum average energy loss in a single event. The WCC and WCR are cut-off energy losses for hard inelastic collision and Bremsstrahlung emission, respectively [27]. The C1 and C2 were set to 0.2 for the increased simulation speed. The WCC and WCR were set to 50 eV for the detailed simulation. The 50 eV is the lowest value for the pyPENELOPE that the user can select. A such low value of WCC and WCR may increase the simulation time. However, it promotes the reliability of the simulation by calculating the possible interaction contributions at low energies.

Similarly, the absorption energies were also set to 50 eV, and default interaction forcing was utilised during the simulation [28]. The default interaction forcing in the pyPENELOPE contains preternaturally enhancing the probability of inner-shell ionisation and bremsstrahlung emission and assigning proper statistical weights to the created secondary particles in such a way that the simulation outcomes stay unbiased [23]. It should be noted that although the pyPENELOPE can track particles down to 50 eV, the interaction cross sections for energies below 1 keV should be considered semi-quantitative [22]. Nevertheless, the reliability of pyPENELOPE has been tested by several research groups by comparing the simulated and experimental results for X-ray spectra from metal targets [28,29], annihilation photon detection [30,31], k-ratios of thin films [32] and different applications [22]. An office computer performed the simulation with  $i5 \times 3.2$  GHz CPU and 8 GB RAM under windows operating systems.

### 3. Results and Discussion

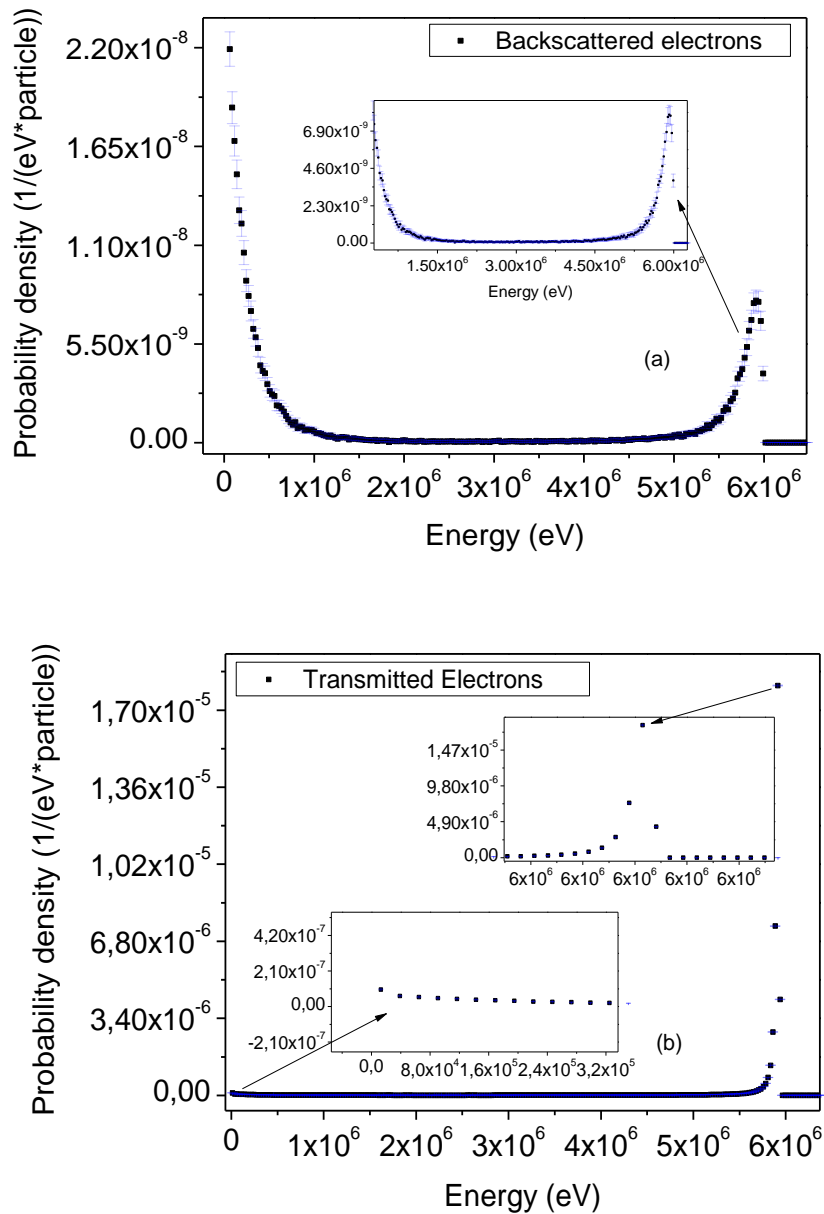
The absorbed, backscattered, and transmitted radiation fractions from the dosimeter structure were obtained after simulation of  $8.2 \times 10^8$  electrons and their distributions were estimated via pyPENELOPE Monte Carlo code. The fractions of these parameters are listed in Table 1. The absorption fraction of the primary particles is 0.00014 with a low uncertainty factor. The dosimeter structure absorbs only 0.014% of the 6 MeV incident electrons. Similarly, the transmission percentage of the radiation was also estimated to be  $102\% \pm 0.022\%$ . This transmission value is the sum of the transmitted primary 6 MeV electrons and secondary irradiations emitted from the interaction of primary 6 MeV electrons with the dosimeter structure. Considering the simulation results, almost 99% of the primary 6 MeV electrons were transmitted from the dosimeter structure, and the remaining transmission values are contributions of the secondary radiations. The fraction of the transmitted secondary electrons is also tabulated in Table 1.

**Table 1.** Various results of the simulated primary and secondary irradiations

	Primary Irradiation		Secondary Electron		Secondary Photon	
	Fraction	Uncertainty x $10^{-5}$	Fraction	Uncertainty x $10^{-5}$	Fraction	Uncertainty x $10^{-5}$
<b>Absorbed</b>	0.00014	1.246	-	-	-	-
<b>Backscattered</b>	0.0118	16.07	0.008	10.40	0.004	6.738
<b>Transmitted</b>	1.021	22.52	0.017	16.71	0.060	25.82

The transmission fraction of the generated secondary electrons is only 0.017. On the other hand, roughly 1.18% of the 6 MeV incident electrons is backscattered by the dosimeter structure. The low interaction and scattering fraction values can be attributed to the thin structure of the skin dosimeters. When the electron radiation propagates through the dosimeters, multiple Coulomb scattering interactions may deflect electrons [33]. Coulomb scattering probability of electron irradiation with the matter is also strictly connected to the thickness of the materials where radiation propagates [33,34]. The approximately 170  $\mu\text{m}$ -thick structure of the designed dosimeters significantly decreases the interaction probability of electrons with the matter. Hence, such low fraction values were obtained after simulations. It seems that these calculated fractions would not anomalously increase or decrease the therapeutic dose during clinical applications. The backscattered and transmitted energy distributions of the 6 MeV electron irradiation from the dosimeter surface are illustrated in Figures 2a-b, respectively. These spectra show how incoming electrons energy varies along the path from the source through the detector structure [18]. As depicted in Figure 2a, some portions of the incident 6 MeV electrons are scattered backwards due to the elastic scattering interactions with atoms in the dosimeter structure [15]. Backscattered electrons increase in regions below 1 MeV and near 6 MeV energy. It can be expected that the large numbers of these backscattered electrons locate at low energies. This can be attributed to multiple elastic scattering of the incident electrons. Some of their incident energy is lost after each scattering during electron propagation. This explains why most backscattered electrons leave the sample after losing their energy.

On the other hand, it has been observed that the transmitted electrons' energies are close to the incident energy of 6 MeV, and no complex energy distribution has been observed. The spectra shown in Figure 2b include the secondary electrons transmitted from the dosimeter structure. In the transmitted electron spectra, no significant contribution has been observed from secondary electrons, which can be visible in the low energies and their transmission fraction is very low, as seen in Table 1. It is easy to complete the absorption of these secondary electrons by the dosimeter's surfaces [15]. Hence, they may not be visible in Figure 2b.



**Figures 2.** The energy distributions of the a-) backscattered electrons and b-) the transmitted electrons

Only a vaguely seen increment has been observed in the energy region of the few keV, which may be originated from secondary electrons or transmitted primary electrons after multiple interactions. On the other hand, this observed transmitted characteristic of electrons is an expected property for the dosimeters. The designed dosimeter does not cause multiple transmitted energy regions, which may deviate the therapeutic dose in clinical practices. Photons with various energies can be generated, resulting in the interaction between incident electrons and materials in the dosimeter. These generated photons can be classified as radiation contamination for dosimeter application [35]. In this aspect, potential radiation contamination consists of the generated x-rays, including the continuum (Bremsstrahlung), characteristics and fluorescence X-rays. Specifying these secondary photon irradiations was also crucial for the dosimeter application, which can lead to unfavourable side effects, e.g., a higher risk of secondary malignancy formation after the radiotherapy.

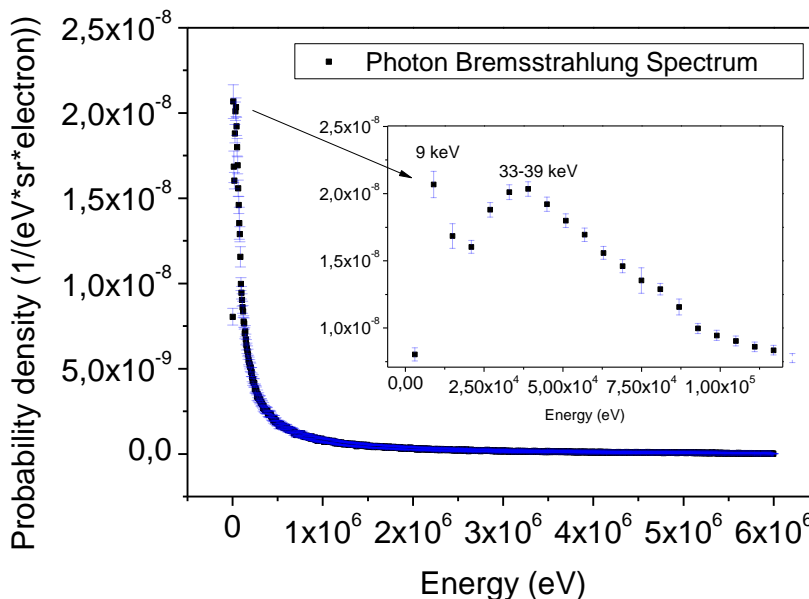


**Figure 3.** The energy distributions of the Bremsstrahlung X-ray spectra

The Bremsstrahlung X-ray radiation spectra are depicted in Figure 3. The Bremsstrahlung background radiation becomes more visible as X-ray energies below 100 keV. A peak at 9 keV was observed in the Bremsstrahlung background, which may correspond to the characteristic X-rays of the Au electrodes [36].

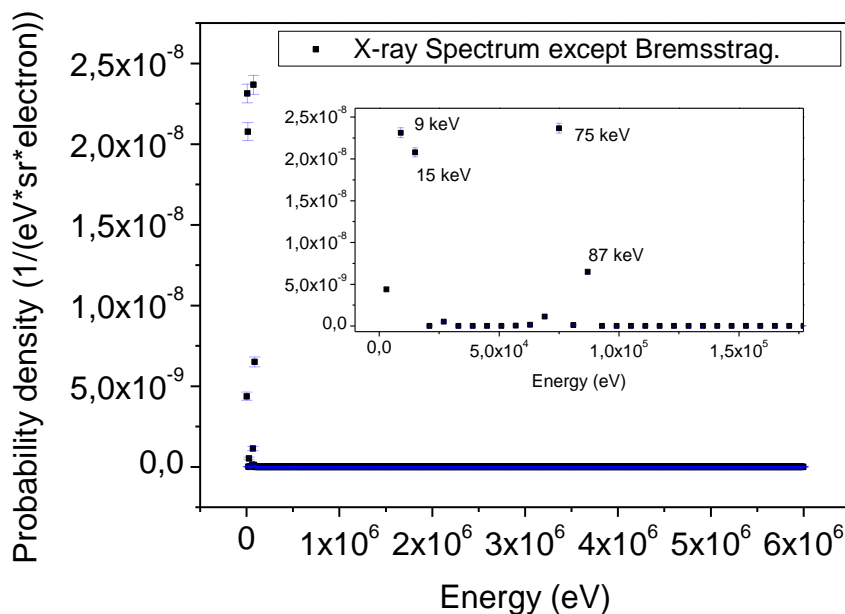


**Figure 4.** The energy distribution of generated photon contamination from the dosimeter surface

The generated X-ray spectra obtained after the simulation is depicted in Figure 4. These distributions in Figure 4 include the photons generated from electron interactions such as fluorescent X-rays but excluded Bremsstrahlung. The observed peaks on the spectra occur owing to the X-ray scattering characteristics of materials in dosimeter structure and the relatively low energy of X-ray fluorescence [37]. The backscattering and transmission ratios of the secondary photons are listed in Table 1. The transmission ratio is essential due to the high penetrating distance of the X-rays into the deeper tissue

levels. Only 6.0 % per cent of the generated secondary photons were transmitted to the tissue side of the dosimeters. It is also worth noting that the quantity of secondary photons generated per incident electron is at least two orders of degrees smaller than that of transmitted electrons (see probability density axes in Figure 2b and Figure 3.

Moreover, the interaction mean free paths for photons are characteristically much higher than electrons [34]. Therefore, these secondary photons' impact on the therapeutic dose is presumably negligible [34]. Nevertheless, it exhibits minimal risk for deep healthy tissues. The angular distributions of the emerging electrons and photons with any energy generated via interactions between incident electrons and dosimeter materials are illustrated in Figure 5. The schematic design of the simulation, including the polar angle distribution [23], has also been depicted in the left corner of Figure 5.

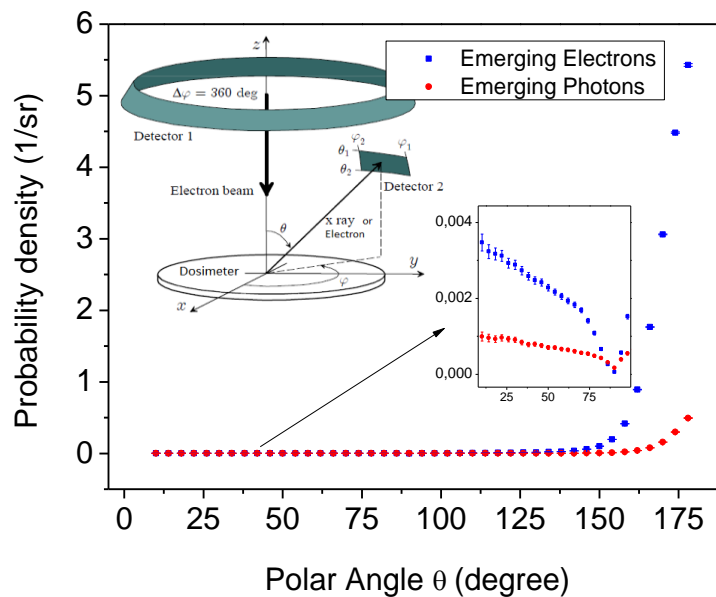


**Figure 5.** Polar angle dependency of emerging photons and electrons emitted from the dosimeter with any energy

The polar angles from zero to 90 degrees contain backscattered secondary photon and electron irradiations. It has been observed that at less than 90 degrees, the distribution varies very slowly with the angles. In addition, the backscattered probability/count of the second irradiation is very low. On the other hand, the polar angles from 90 to 180 degrees contain the transmitted secondary photon and electron irradiations which may cause the enhancement of the therapeutic doses on the patient body. The secondary photons were scattered in almost the same direction as the incident electron irradiations, as depicted in Figure 5.

On the other hand, the scattered region of the secondary electrons was a bit broad than the secondary photons. Due to the multiple elastic scattering, some portion of the secondary electrons deviated roughly 30 degrees from the target tissue. Nevertheless, the simulation results demonstrate that considering probability density, large numbers of emerging electrons are still oriented to the target tissue.

#### 4. Conclusion

The fraction and energy distributions of the incident 6 MeV electrons and generated secondary electron and photon radiations scattered from novel lead oxide-based flexible skin dosimeters have been

investigated in detail. Considering simulation results, almost 99% of the primary 6 MeV electrons were transmitted from the dosimeter structure. The transmission fraction of the generated secondary electrons is only 0.017. On the other hand, roughly 1.18% of the 6 MeV incident electrons is backscattered by the dosimeter structure. The low scattering fraction values can be attributed to the thin structure of the skin dosimeters. No abnormal changes were observed in the fraction and energy distribution of the transmitted incident electrons.

Moreover, only 6.0 % per cent of the generated secondary photons were transmitted to the tissue side of the dosimeters. The observed peaks on the secondary photon spectra occur owing to the X-ray scattering properties of materials in the dosimeter structure. It is also worth noting that the quantity of secondary photons generated per incident electron is at least two orders of degrees smaller than the number of transmitted electrons, i.e., these secondary photons have limited effects on the therapeutic doses. Angular distributions of the scattered secondary radiation are not anomalous large to significantly enhance the radiation dose on the surrounding healthy tissue. The simulated results have demonstrated that the designed skin dosimeters may not significantly cause a large dose enhancement/decrement in the patient body. Hence, the lead oxide-based flexible skin dosimeter has great potential to be used as a measurement device during electron therapy.

### Author Contributions

The author read and approved the last version of the paper. The author performed all simulations and discussions.

### Conflicts of Interest

The author declares no conflict of interest.

### Acknowledgement

The author would like to thank Mehmet Tanrikulu Vocational School Bolu Abant Izzet Baysal University for providing an office-type computer to perform the simulation. The author also would like to thank pyPENELOPE development group (<http://pypenelope.sourceforge.net>) for the open source and free usage of the simulation package.

### References

- [1] P. E. Huber, J. Debus, D. Latz, D. Zierhut, M. Bischof, M. Wannemacher, R. Engenhart-Cabillic, *Radiotherapy for advanced adenoid cystic carcinoma: neutrons, photons or mixed beam?*, *Radiotherapy and Oncology*, 59(2), (2001) 161–167.
- [2] N. Adnani, B. G. Fallone, *Neutron therapy using medical linacs*, in: J. D. Enderle (Ed.), *Proceedings of the 22nd Annual International Conference of the IEEE Engineering in Medicine and Biology Society 2020*, Chicago, USA, 2000, pp. 133–136.
- [3] W. Kawakami, S. Takamatsu, M. Taka, K. Ishii, T. Nakaichi, K. Funamoto, K. Yokoyama, *Factors associated with radiation pneumonitis in patients receiving electron boost radiation for breast-conserving therapy: a retrospective review*, *Advances in Radiation Oncology*, 5(6), (2020) 1141–1146.

- [4] S. C. S. Cunha, L. A. V. Carvalho, P. C. Canary, M. Reisner, K. B. Corgozinho, H. J. M. Souza, A. M. R. Ferreira, *Radiation therapy for feline cutaneous squamous cell carcinoma using a hypofractionated protocol*, *Journal of Feline Medicine and Surgery*, 12(4), (2010) 306–313.
- [5] S. Hyodynmaa, A. Gustafsson, A. Brahme, *Optimisation of conformal electron beam therapy using energy- and fluence-modulated beams*, *Medical Physics*, 23(5), (1996) 659–666.
- [6] J. Narbutt, A. Chrusciel, A. Rychter, J. Fijuth, A. Sysa-Jedrzejowska, A. Lesiak, *Persistent improvement of previously recalcitrant Hailey-Hailey disease with electron beam radiotherapy*, *Acta Dermato-Venereologica*, 90(2), (2010) 179–182.
- [7] A. M. Saadeldin, A. M. Elwan, *Characterisation of irregular electron beam for boost dose after whole breast irradiation*, *Reports of Practical Oncology and Radiotherapy*, 25(2), (2020) 168–173.
- [8] M. J. Han, S. W. Yang, S. I. Bae, Y. M. Moon, W. Jeon, C. W. Choi, S. K. Park, J. Y. Kim, *Evaluation of monoxide film-based dosimeters for surface dose detection in electron therapy*, *Plos One*, 16(5), (2021) Article ID: e0251441, 1–10.
- [9] L. E. Court, R. B. Tishler, A. M. Allen, H. Xiang, M. Makrigiorgos, L. Chin, *Experimental evaluation of the accuracy of skin dose calculation for a commercial treatment planning system*, *Journal of Applied Clinical Medical Physics*, 9(1), (2008) 29–35.
- [10] D. Manigandan, G. Bharanidharan, P. Aruna, K. Devan, D. Elangovan, V. Patil, R. Tamilarasan, S. Vasanthan, S. Ganesan, *Dosimetric characteristics of a MOSFET dosimeter for clinical electron beams*, *Physica Medica-European Journal of Medical Physics*, 25(3), (2009) 141–147.
- [11] A. G. Dias, D. F. S. Pinto, M. F. Borges, M. H. Pereira, J. A. M. Santos, L. T. Cunha, J. Lencart, *Optimisation of skin dose using in-vivo MOSFET dose measurements in bolus/non-bolus fraction ratio: A VMAT and a 3DCRT study*, *Journal of Applied Clinical Medical Physics*, 20(2), (2019) 63–70.
- [12] K. Oh, M. Han, J. Kim, Y. Heo, K. Kim, G. Cho, Y. Song, S. Cho, S. Heo, J. Kim, S. Park, S. Nam, *Flexible X-ray detector for automatic exposure control in digital radiography*, *Journal of Nanoscience and Nanotechnology*, 16, (2016) 11473–11476.
- [13] M. J. Han, S. W. Yang, S. I. Bae, Y. M. Moon, S. U. Heo, C. W. Choi, S. K. Park, J. Y. Kim, *Evaluation of attenuation rate error for optimisation of skin dosimeter in electron beam therapy*, *Journal of Instrumentation*, 15, (2020) Article ID: P07012.
- [14] N. Chaudhary, A. Singh, D. K. Aswal, A. K. Debnath, S. Samanta, S. P. Koiry, S. Sharma, K. Shah, S. Acharya, K. P. Muthe, S. C. Gadkari, *Electron beam modified zinc phthalocyanine thin films for radiation dosimeter application*, *Synthetic Metals*, 231, (2017) 143–152.
- [15] P. Dondero, A. Mantero, V. Ivanchenko, S. Lotti, T. Mineo, V. Fioretti, *Electron backscattering simulation in Geant4*, *Nuclear Instruments & Methods in Physics Research Section B-Beam Interactions with Materials and Atoms*, 425, (2018) 18–25.
- [16] J. T. Rakowski, S. S. Laha, M. G. Snyder, M. G. Buczek, M. A. Tucker, F. C. Liu, G. Z. Mao, Y. Hillman, G. Lawes, *Measurement of gold nanofilm dose enhancement using unlaminated radiochromic film*, *Medical Physics*, 42(10), (2015) 5937–5944.
- [17] T. Shimozato, K. Okudaira, H. Fuse, K. Tabushi, *Monte Carlo simulation and measurement of radiation leakage from applicators used in external electron radiotherapy*, *Physica Medica-European Journal of Medical Physics*, 29(4), (2013) 388–396.

- [18] A. Kahraman, S. Kaya, A. Jaksic, E. Yilmaz, *A comprehensive study on the photon energy response of RadFET dosimeters using the PENELOPE Monte Carlo code*, Radiation Effects and Defects in Solids, 170(5), (2015) 367–376.
- [19] J. Sempau, P. Andreo, *Configuration of the electron transport algorithm of PENELOPE to simulate ion chambers*, Physics in Medicine and Biology, 51(14), (2006) 3533–3548.
- [20] M. Asai, M. A. Cortés-Giraldo, V. Giménez-Alventosa, V. Giménez Gómez, F. Salvat, *The PENELOPE physics models and transport mechanics. implementation into Geant4*, Frontiers in Physics, 9, (2021) Article ID: 738735, 1–20.
- [21] F. Salvat, Penelope: A Code System for Monte Carlo Simulation of Electron and Photon Transport, OECD Nuclear Energy Agency, 2019.
- [22] X. Llovet, F. Salvat, *PENEPMA: a Monte Carlo programme for the simulation of X-ray emission in EPMA*, IOP Conference Series: Materials Science and Engineering, 109, (2016) Article ID: 012009, 1–13.
- [23] X. Llovet and F. Salvat, *PENEPMA: A Monte Carlo program for the simulation of X-Ray emission in electron probe microanalysis*, Microscopy and Microanalysis, 23(3), (2017) 634–646.
- [24] J. S. Choi, D. W. Ko, J. Y. Seo, J. H. Nho, J. H. Chang, S. T. Lee, J. Y. Jung, M. J. Lee, *Electrical and chemical sensing properties of a printed indium-tin-oxide film for the detection of hazardous and noxious substances*, Journal of the Korean Physical Society, 76(11), (2020) 1005–1009.
- [25] S. W. Yang, M. J. Han, S. K. Park, J. B. Chung, J. K. Kang, T. S. Yu, J. E. Rah, J. K. Kim, M. W. Lee, J. Y. Kim, *Development and evaluation of a monoxide-based flexible skin dosimeter for radiotherapy at photon energies*, Journal of Instrumentation, 16, (2021) Article ID: P07056.
- [26] D. F. Craft, J. Lentz, M. Armstrong, M. Foster, J. Gagneur, D. Harrington, S.E. Schild, M. Fatyga, *Three-dimensionally printed on-skin radiation shields using high-density filament*, Practical Radiation Oncology, 10(6), (2020) e543–e550.
- [27] C. Y. Yi, S. H. Hah, M. S. Yeom, *Monte Carlo calculation of the ionisation chamber response to Co-60 beam using PENELOPE*, Medical Physics, 33(5), (2006) 1213–1221.
- [28] P. Adamson, C. Cannon, S. Williams, *Bremsstrahlung produced by 5 keV electrons incident on BeO and NaCl*, Nuclear Instruments & Methods in Physics Research Section B-Beam Interactions with Materials and Atoms, 490, (2021) 43–47.
- [29] D. Gonzales, B. Cavness, S. Williams, *Angular distribution of thick-target Bremsstrahlung produced by electrons with initial energies ranging from 10 to 20 keV incident on Ag*, Physical Review A, 84, (2011) Article ID: 052726.
- [30] L. Tao, J. H. Wang, M. Esmaelpour, C. S. Levin, *Simulation studies to understand sensitivity of an optical property modulation-based radiation detection concept for PET*, IEEE Nuclear Science Symposium and Medical Imaging Conference Proceedings (Nss/Mic) 2018, Sydney, NSW, Australia, 2018 Article ID: 178.
- [31] L. Tao, D. Jeong, J. H. Wang, Z. Adams, P. Bryan, C. S. Levin, *Simulation studies to understand sensitivity and timing characteristics of an optical property modulation-based radiation detection concept for PET*, Physics in Medicine and Biology, 65, (2020) Article ID: 215021, 1–17.
- [32] P. Statham, X. Llovet, P. Duncumb, *Systematic discrepancies in Monte Carlo predictions of k-ratios emitted from thin films on substrates*, IOP Conference Series: Materials Science and Engineering, 32, (2012) Article ID: 012024, 1–7.

- [33] O. Lundh, C. Rechatin, J. Faure, A. Ben-Ismaïl, J. Lim, C. De Wagter, W. De Neve, V. Malka, *Comparison of measured with calculated dose distribution from a 120-MeV electron beam from a laser-plasma accelerator*, Medical Physics, 39(6), (2012) 3501–3508.
- [34] F. Salvat-Pujol, H. O. Jeschke, R. Valenti, *Simulation of electron transport during electron-beam-induced deposition of nanostructures*, Beilstein Journal of Nanotechnology, 4, (2013) 781–792.
- [35] H. R. Baghani, B. Aminafshar, *In-field radiation contamination during intraoperative electron radiation therapy with a dedicated accelerator*, Applied Radiation and Isotopes, 155, (2020) Article ID: 108918.
- [36] Y. H. Li, Z. An, J. J. Zhu, L. Li, *Characteristic X-ray yields and cross sections of thick targets of Al, Ti, Zr, W and Au induced by keV-electron impact*, Acta Physica Sinica, 69(13), (2020) Article ID: 133401, 1–13.
- [37] W. Kim, J. Jang, D. H. Kim, *Monte Carlo simulation for the analysis of various solid samples using handheld X-ray fluorescence spectrometer and evaluation of the effect by environmental interferences*, Spectrochimica Acta Part B-Atomic Spectroscopy, 180, (2021) Article ID: 106203, 1–9.